

Separate and Detailed Treatment of Absolute Signal and Noise Enables NMR Under Adverse Circumstances

A. Guinness,¹ Alec A. Beaton,¹ and John M. Franck¹

¹*Department of Chemistry, Syracuse University, Syracuse, NY 13210, USA**

(Dated: Thursday 7th March, 2024)

When deploying a spectrometer in an adverse environment, such as during a typical ODNP experiment or experiments that require low-volume low-field measurements, a clear and modern protocol for characterizing and quantifying the absolute signal and noise levels proves essential. This paper provides such a protocol. It also highlights the clarity and insight that comes from (1) discussing NMR signal intensities in (conserved) units of square root instantaneous power that are derived from a theory and notation developed initially for ESR spectroscopy; as well as (2) characterizing the spectral distribution of the noise.

Crucially, the strategy introduced here applies not only to ODNP measurements, but to all low-field NMR. Low-field NMR offers immense flexibility: it enables integration with other instrumentation and deploys in practical applications not accessible to higher-field instrumentation. More generally, the protocol introduced here should apply to a wide range of instruments, and should prove especially useful in cases subject to design constraints that requires integration with multiple other modules that are not dedicated to NMR but that control other forms of spectroscopy or other crucial aspects of the measurement. However, in the specific case of ODNP, this protocol demonstrates that the absolute signal and noise level can be estimated from the clarified theory presented here, and uses that theory to identify the inefficient distribution of fields in the hairpin loop probe as the main remaining bottleneck for the improvement of low-field low-volume ODNP SNR.

I. Introduction

New physical techniques and modern technologies are reinvigorating the magnetic resonance community. For example, ODNP performs detailed analyses of hydration dynamics on the surfaces and interiors of samples with intricate structure at the nanoscale: ranging from proteins to reverse micelles and porous materials [1? – 7]. However, ODNP imposes specific requirements on the experimental setup. In particular, while integration with a standard cw ESR spectrometer offers clear advantages, it is reasonably well recognized that the ESR instrumentation potentially introduces a sea of noise that renders the isolation and optimization of signal increasingly difficult. ODNP thus, overall, serves as a good example of what can be termed NMR under adverse circumstances. However, many situations call for NMR under adverse circumstances, including single-sided NMR for materials studies [8], NMR in the presence of electromagnetic noise [9], NMR in oil bore wells [10, 11], surface NMR and MR sounding techniques in hydrogeological investigations [9, 12, 13], and portable NMR [14].

Common strategies to improve the SNR include utilizing pre-polarization pulses [13, 15], empirical mode decomposition [12], suppression algorithms [16], incorporating better shielding [8, 17–20], improving grounding [19], bandwidth filters, additional sweep coils [21], and improving the amplifier noise figures [14, 22–24], while the post-processing stage of data analysis can also improve the SNR [25–28]. However, while the field has become quite crowded with the development of an

ever-increasing array of designs, the authors are aware of few clear and robust protocols to aid in the development of these designs. This situation is exacerbated by the fact that actions that solve noise issues on one system – *e.g.* (for ODNP), adding hardware to ground transmission lines to the waveguide, [6, 7, 29] moving to an older model of the commercial electromagnet power supply, deriving magnetic field from permanent magnets [1, 8], or developing customized hardware [30?] do not always yield the same effect in different laboratory environments. Practically, even the best new hardware designs in the literature might not be compatible with the requirements, capabilities, or environment of a different laboratory [31–33]. Therefore, the community requires not just new instrumental schematics, but also (as provided here) a simple and flexible protocol for systematically diagnosing and mitigating the sources of noise and for identifying the elements of the design that limit the absolute signal intensity.

The optimization of signal to noise in the NMR experiment can sometimes be treated as an art, when, in fact, the fundamental science is well established and lacking only a widely applicable procedure for implementation. This paper provides a protocol, theory, and software toolkit for separately quantifying the noise and the signal. Common off-the-shelf equipment, especially when coupled with open-source software, can easily characterize the noise over a broad bandwidth (sec. IV.1.A). Digitization of the noise power spectral density identifies the relative contribution of various noise sources in the laboratory according to their respective spectral fingerprints (sec. IV.1.B). Noise mitigation efforts can then be reproducibly tested until the noise approaches the thermal noise limit (sec. IV.1.E). Characterization of the

* jmfranck@syr.edu

transceiver response then leads to quantitative agreement between the noise measured at the transceiver vs. with standard off-the-shelf equipment (sec. IV.2.B). In particular, this allows identification and correction for the idiosyncrasies the transceiver, and avoidance of extra noise introduced by the transceiver (sec. IV.2.C). Finally, the adapted theory can make a very accurate prediction of the signal to noise that will be observed in the customized system, and also identify the most productive way to improve the SNR (sec. IV.3). *In the specific context of ODNP, we show that this protocol makes it possible to measure the enhancements arising from very low concentrations of spin label on a hardware system where this would not otherwise be possible.*

II. Theory

This section first recapitulates the theory that predicts the absolute NMR signal intensity. In particular, it emphasizes the importance of the concept of reciprocity by Hoult[33, 34], while pointing out that this concept naturally integrates with two key concepts from the ESR literature: the conversion factor (Λ)[29, 35], and the treatment Mims' treatment of the field distribution [36]. For completion, it then reviews the concept of Johnson-Nyquist Noise. Finally, because part of the results emphasize the benefit of characterizing the power spectral density of the noise, it provides equations that can generate such plots from data acquired on a standard digital capture oscilloscope.

II.1. The Conversion Factor

The term the ESR literature denotes as the ‘‘conversion factor’’ (i.e., ‘‘efficiency parameter’’)[35–38], Λ , with units $[\text{T}/\sqrt{\text{W}}]$, gives the ratio of useful magnetic rf field to the pulse power:

$$\Lambda = \frac{B_{1,avg}}{\sqrt{P_{tx,rms}}} \quad (1)$$

where $P_{tx,rms}$ is the RMS transmitted power [W] required to achieve a rotating frame magnetic field of $B_{1,avg}$ (where $B_{1,avg}$ [T] is averaged over the sample). The value of Λ can be determined from a standard calibration of the 90° pulse time, namely:

$$\Lambda = \frac{\pi}{2t_{90}\gamma\sqrt{P_{tx,rms}}} \quad (2)$$

where t_{90} [s] gives the length of a 90° pulse when the pulse power is set to $P_{tx,rms}$, and γ is the gyromagnetic ratio $[\text{rad} \cdot \text{s}^{-1} \cdot \text{T}^{-1}]$.

II.2. Reciprocity in terms of Λ

With the assumption that the spins are uniformly excited,

$$\xi_{sig,p} = \left(\frac{B_{1,lab}}{I_{coil,p}} \right) \omega M_0 V_s \quad (3)$$

gives the peak voltage of the signal ($\xi_{sig,p}$), where ω is the Larmor frequency $[\text{rad}/\text{s}]$, V_{sample} is the volume

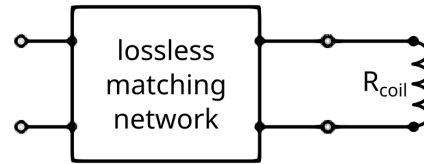


FIG. 1. Example of a circuit with a coil attached to a lossless matching network

of the sample $[m^3]$, M_0 is the nuclear magnetization ($N\omega\gamma\hbar^2 I(I+1)/3k_B T$ N is the number of spins per unit volume, I is the quantum number of the spin (e.g., $I = 1/2$ for 1H , 1 for 2H), and T is the temperature $[K]$), $B_{1,lab}$ is the average magnetic field that is generated perpendicular to both the spins and the field when a current of $I_{coil,p}$ flows through the coil; note that the ratio $B_{1,lab}/I_{coil,p}$ appears in the expression for $\xi_{sig,p}$ as a consequence of the principal of reciprocity. (Eq. 3 is equivalent to eq 4 of Hoult [34], with $K = 1$). Specifically, eq. 3 gives the peak voltage generated during an echo with minimal relaxation.

Of course, $\xi_{sig,p}$ is not conserved when a lossless matching network is attached to the coil. However, the square root of the peak signal power

$$\sqrt{P_{sig,p}} = \frac{\xi_{sig,p}}{\sqrt{R_{coil}}} = \left(\frac{B_{1,lab}}{I_{coil,p}} \right) \frac{\omega M_0 V_s}{\sqrt{R_{coil}}} \quad (4)$$

where R_{coil} is the resistance of the coil, is conserved. The same $\sqrt{P_{sig,p}}$ will be measured at the terminals of any lossless matching network. For the circuit of fig. 1, the only source of resistive impedance is R_{coil} , and it can be noted that

$$\frac{B_{1,lab}}{I_{coil,p}\sqrt{R_{coil}}} = \frac{(2B_{1,avg})}{(\sqrt{2}I_{coil,rms})\sqrt{R_{coil}}} = \sqrt{2}\Lambda$$

where $B_{1,lab} = 2B_{1,avg}$ accounts for the two counter-rotating components of the magnetic field, while $I_{coil,rms} = I_{coil,p}/\sqrt{2}$ converts from current amplitude to rms current. Substituting this expression into eq. 4 yields

$$\sqrt{P_{sig,p}} = \sqrt{2}\omega M_0 V_{sample}\Lambda \quad (5)$$

This expression also holds for any circuit that can be proved equivalent to fig. 2, since the attenuation will be reflected in a concomitant reduction of Λ relative to the circuit with the lossless matching network. Eq. 5 quantifies in a more convenient form what is already stated in a different form by Hoult [33, 34] and known in ESR spectroscopy:

Λ is not merely an expression of the probe efficiency, but also quantifies the sensitivity with which it detects spin precession.

II.3. Factors affecting Λ

A careful analysis of existing literature (both NMR and ESR) concludes that only three quantities control the

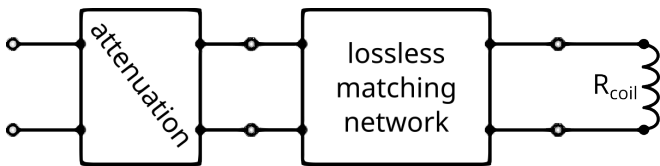


FIG. 2. Example of a circuit with the same coil attached to a lossy matching network

value of Λ : the volume of the sample, the Q -factor, and a unitless factor that we term the “field distribution factor” η' (which is related to, but in most contexts different from the more common “filling factor”)[31, 33, 35, 37, 39–41].

As noted by Mims [36], the energy stored in an impedance-matched resonant rf circuit can be *exactly* quantified using either the magnetic field energy or the definition of the Q -factor, leading to the relation:

$$\frac{1}{2\mu} \iiint |\mathbf{B}_1(\mathbf{r})|^2 d\mathbf{r} = \frac{QP_{tx,rms}}{\omega} \quad (6)$$

where the three-dimensional \mathbf{r} integral is over all space, ω is the resonance frequency, and $P_{tx,rms}$ is the power used to generate the \mathbf{B}_1 field. Eq. 6 defines $\mathbf{B}_1(\mathbf{r})$ distinctly from $B_{1,avg}$ in eq. 1 and integrates over all magnetic fields generated by all circuit elements within the impedance matched probe. In contrast, $B_{1,avg}$ represents the average only over the portion of the rf field capable of generating nutation:

$$2B_{1,avg} = \frac{1}{V_{sample}} \iiint_{V_{sample}} \frac{|\mathbf{B}_0(\mathbf{r}) \times \mathbf{B}_1(\mathbf{r})|}{|\mathbf{B}_0(\mathbf{r})|} d\mathbf{r} \quad (7)$$

where the vector \mathbf{B}_0 is the static magnetic field. The factor of 2 accounts for the fact that the definition of $B_{1,avg}$ includes only one of the two counter-rotating components of the field, as opposed to the full strength of the oscillating rf in the laboratory frame.[?]]

Mims’ analysis [36] was developed for resonators that even lacked well-defined lumped circuit elements, such as an inductive coil. In various contexts, such an analysis can offer insight; for example, in ODNP, a hairpin coil has a very small inductance that one can suspect suffers competition from stray inductances within the rest of the tuning circuitry. Most literature estimates a “filling factor” (η) by noting, *e.g.* the extent to which a sample fills a sample coil[35], and there are many variations on this theme [34, 41]. However, by integrating elements from Mims’ analysis, one can see that the definition

$$\eta' = \frac{4B_{1,avg}^2 V_{sample}}{\iiint |\mathbf{B}_1(\mathbf{r})|^2 d\mathbf{r}} \quad (8)$$

proves more general and/or accurate than other options. Like the value of η , η' is unitless: both the numerator and denominator have units of $[\text{T}^2 \cdot \text{m}^3]$, with field in the lab frame. As the authors are unaware of previous literature that gives a name to this exact term, to discriminate from

other options, η' is referred to here as the “field distribution factor,” however note that it corresponds exactly to the quantity V_s/V_c in the nomenclature of Mims [36] (where $V_s = V_{sample}$). Importantly, note that the original V_c of Mims is *not* the coil volume (or cavity volume) or any real physical volume; it is rather the “effective cavity volume” and defined with a field integral like eq. 8.

In the idealized case where the only rf magnetic field that exists outside the transmission line exists inside the coil volume (where it would then be equal to $2B_{1,avg}$), η' would correspond to the extent to which the sample fills the inside of the coil: *i.e.* under such idealized conditions, one would find $\eta \approx \eta'$. However, as the results will indicate, very constrained designs such as the hairpin loop utilized in many X-band ODNP experiments fall very far from this condition.

By substituting eq. 6 into eq. 8, eq. 1 can be rewritten to show the relationship between the conversion factor, the field distribution factor, the Q factor, and the volume of the sample:

$$\Lambda = \sqrt{\frac{\eta' \mu Q}{2\omega V_{sample}}} \quad (9)$$

which naturally resembles many equations that one finds in the probe design literature [41], though from following the analysis of Mims [36] and the resulting definitions, it should be exact and generalizable to unusual probe designs.

Finally, note that the expression (arising from substituting eq. 2 into eq. 9 and rearrangement)

$$\eta' = \left(\frac{\pi^2 2\omega}{4\mu\gamma^2} \right) \left(\frac{V_{sample}}{t_{90}^2 Q P_{tx,rms}} \right) \quad (10)$$

yields η' as a function of the physical constants (*e.g.*, ω , μ , γ , and V_{sample}) and quantities that can be measured (*e.g.*, t_{90} , Q , and $P_{tx,rms}$).

II.4. Johnson-Nyquist Noise

Of course, this article concerns itself, in part, with the origins of noise that can obscure low-field NMR signal. The Johnson-Nyquist noise [42] that an impedance-matched receiver detects when connected to an impedance-matched probe is given by [37]:

$$\frac{P_{noise}}{\Delta\nu} = k_B T \quad (11)$$

where k_B is the Boltzmann constant [J/K], T is the temperature [K], and $\Delta\nu$ is the bandwidth [Hz] of the detector. The Johnson-Nyquist noise is white noise – *i.e.* this equation does not vary with the center frequency of the detector [22, 43]. Of course, low-noise amplifiers will also add a noise level in keeping with their noise temperature, as governed by the Friis equation,

$$F_{total} = F_1 + \frac{F_2 - 1}{G_1} + \frac{F_3 - 1}{G_1 G_2} + \dots + \frac{F_n - 1}{G_1 G_2 \dots G_{n-1}} \quad (12)$$

where F_n is the noise factor of the n th stage of a multistage amplifier, and G_n is the gain of the n th stage of the multistage amplifier[44]. As a large portion of the results focus on identifying and reducing EMI; we refer to the noise that results from eq. 11 and the LNA noise as the “thermal noise limit.”

II.5. Standard Equations for Signal Processing

Several equations assist in relating real-valued oscilloscope data to quadrature data and/or noise power spectral densities.

The standard analytical signal transformation effectively converts real-valued signal $s(t)$ into quadrature signal $s_a(t)$. Specifically,

$$\tilde{s}(\nu) = \sum_{t=0}^{t=t_{acq}} e^{+i2\pi\nu t} s(t) \Delta t \quad (13)$$

$$s_a(t) = \sum_{\nu=0}^{\nu=1/2\Delta t} (2 - \delta_{\nu,0}) e^{+i2\pi\nu t} \tilde{s}(\nu) \Delta \nu \quad (14)$$

where $\delta_{\nu,0}$ is zero except at $\nu = 0$ (where it is 1), Δt is the spacing between the time domain points, and the spacing between the frequency domain points is given by $\Delta \nu = 1/(t_{acq} + \Delta t)$. (Note that eq. 14 corresponds to multiplication in the frequency domain by a Heaviside function and downsampling.) The analytic signal provides instantaneous amplitude ($|s_a(t)|$), power ($|s_a(t)|^2$), and phase ($\text{angle}(s_a(t))$) information, while $\Re[s_a(t)] = s(t)$ (sinc interpolated to twice the sampling rate) corresponds to the signal captured on the oscilloscope.

There should be a correspondence between signal digitized on the NMR receiver ($s_{transceiver}(t)$) and the analytic signal derived from oscilloscope data. Specifically,

$$s_{transceiver}(t) = (s_a(t) \exp(-i2\pi\nu_c t)) \otimes f_{DF}(t) \quad (15)$$

where ν_c is the carrier frequency of the NMR signal (the digital equivalent of a local oscillator (LO)), $f_{DF}(t)$ is the digital convolution filter, and \otimes represents the convolution operation.

When starting from oscilloscope or transceiver data in the time domain, a convolution (normalized Gaussian of width σ) smooths the square of the complex magnitude of the Fourier transform, which is divided by the characteristic impedance and the length of the acquisition to convert to a PSD ($P_{noise}(\nu)$) with units [W/Hz] – *i.e.*:

$$\begin{aligned} P_{noise}(\nu) &= \frac{1}{t_{acq} Z_c \sigma N \sqrt{2\pi}} \sum_{i=1}^N \sum_{\nu'} e^{-(\nu-\nu')^2/2\sigma^2} \left| \sum_{t=0}^{t_{acq}} e^{-i2\pi\nu' t} s_a(t) \Delta t \right|^2 \Delta \nu \\ &= \frac{1}{t_{acq} Z_c \sigma N \sqrt{2\pi}} \sum_{i=1}^N e^{-\nu^2/2\sigma^2} \otimes \left| \sum_{t=0}^{t_{acq}} e^{-i2\pi\nu t} n_i(t) \Delta t \right|^2 \Delta \nu \end{aligned} \quad (16)$$

where $n_i(t)$ [V] is the time-domain noise voltage, Z_c [Ω] the characteristic impedance of the transmission line (typically 50 Ω), t_{acq} [s] the length of the acquisition, σ [Hz] the convolution width, and N is the number of averaged scans. Even though noise is, of course, phase

incoherent, P_{noise} still adds linearly, allowing for the signal averaging or convolution that are important to clarifying the shape of P_{noise} and deriving meaning from it. Note that, throughout, noise PSDs acquired from (real valued) oscilloscope data are presented with the negative frequency portion of the PSD discarded, as it is a mirror image of the positive frequencies.

III. Methods

III.1. Samples

A 4.8 μL sample of 27 mM 4-hydroxy-2,2,6,6-tetramethylpiperidine-1-oxyl (TEMPO) sample (Toronto Research Chemical) in deionized water was loaded into a capillary tube with an inner diameter of 0.6 mm, and flame sealed for use as the standard sample, with a typical relaxation time of about 100 ms.

III.2. Hardware

Roughly following the design shown in [29], the tuning box containing adjustable capacitors for the probe’s tank circuit attaches to the bottom of the ESR cavity (which has a threaded connector) by way of a threaded collar piece that presses against a conductive neck attached to the tuning box to bring it into electrical contact with the shield surrounding the ESR cavity. When in place, a multimeter was used to perform a continuity check between the ground of the ESR cavity and that of the probe.

As fig. 3 shows, the ESR cavity sits between the plates of the electromagnet, attached to a waveguide that connects to a high power microwave source. The bottom of the probe tuning box connects *via* BNC connectors and coaxial cable (RG58/U 20 AWG) to the input of an aluminum enclosure containing the receiver chain: a home-built passive duplexer, two standard LNAs (Mini-Circuits ZFL-500LN+), an analog low-pass filter (Mini-Circuits SLP-21.4+) and (for select measurements) an analog high-pass filter (Crystek Corporation CHPFL-0010-BNC).

When employed, common-mode chokes of the snap-on Ferrite style; that surround the coaxial cable (designed for broadband operation up to 300 MHz) with an inner diameter of 6.35 mm and a typical outer diameter of 12.2 to 19 mm attach to the coaxial cable connecting the tuning box to the receiver pathway enclosure.

The Bruker E500 hardware[35], in conjunction with the XEPR software and Bruker Python API, controls the magnetic field. This setup employs a Hall sensor for magnetic field detection. It is worth noting that every laboratory setup differs in a way that may affect noise generation and transmission[6, 8, 14, 21, 30, 33, 45, 46]. Here by necessity, all the ESR hardware connects to a different circuit (different voltage supply) than the NMR hardware, and a transformer isolates it from the electrical mains supply. While the flooring surface in this instance, is insulating, it rests over continuous metal sheeting.

During typical NMR experiments, the SpinCore RadioProcessor-G serves as the transceiver board in the current lab (fig. 3) and offers a real-time oversampling

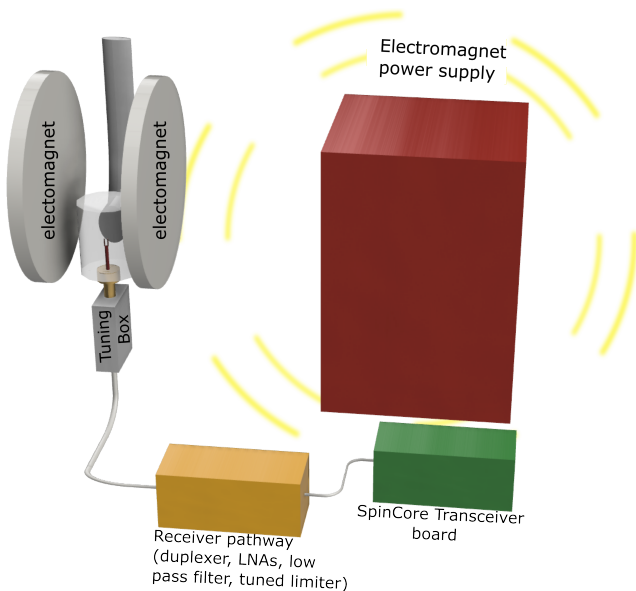


FIG. 3. Instrumental setup: The power supply of the electromagnet (red) sits adjacent to the magnet itself, connected by heavy-gauge DC supply lines (not shown). The silver box labeled “tuning box” contains the the capacitors for the probe circuit, with the hairpin loop rf coil extending upwards through a hole into the ESR cavity. A 1.22 m BNC cable connects the NMR probe to the receiver chain (yellow) before the transceiver board (green) digitizes it. The electromagnet power supply emits interference noise as indicated by the yellow dashed circles. This drawing omits microwave and rf amplifiers and parts of the ESR instrumentation in favor of emphasizing the elements crucial to the receiver pathway.

capability. However, the protocol here is intended to accommodate a variety of possible transceivers that offer oversampling. Note that all communication with the SpinCore transceiver occurs *via* a Python API extension developed by the authors from C language API and examples supplied by the vendor [47].

For an independent off-the-shelf test and measurement equipment, we rely on a minimal set of instrumentation: specifically an oscilloscope (GW-Instek GDS-3254, bandwidths up to 250 MHz, and sampling rates up to 5 GSPS), an Arbitrary Function Generator (GW-Instek AFG-2225), and a handheld Vector Network Analyzer (NanoVNA-H, version 3.5).

III.3. Details of Oscilloscope-Based Noise Measurement

For the widest applicability, this section covers detailed considerations of performing noise PSD measurements with a standard oscilloscope. All data is retrieved with the library available at https://github.com/jmfrancklab/inst_notebooks/ that specifically adopts a strategy of enabling python context blocks for the connection to the oscilloscope, and providing the captured data as an object containing all axis coordinate and unit information (in `pySpecData` format). The strat-

egy should be extensible to a wide range of digital capture oscilloscopes, as well as to spectrum analyzers capable of digital capture (in addition to the direct USB RS232 communication employed here, the libraries also offer context blocks for handling GPIB communications over Prologix connectors). Note that the authors have previously provided a demonstration [5] that the same software and oscilloscope employed here are capable of capturing a phase-cycled spin echo.

For an oscilloscope-based measurement of noise, the receiver chain must include a low-pass filter after the low-noise amplifiers. The sampling rate on the oscilloscope must also exceed twice the high-frequency edge of the low-pass filter (*e.g.* in fig. 4 the sampling rate must exceed 70 MHz). A plot of the noise PSD (processed with eq. 16) will then clearly display the edge of the band-pass filter, as shown by the red, green, and gold curves in fig. 4, which was acquired with a 25 MHz low-pass filter in place.

While standard oscilloscope measurements offer an easy comparison to, and smooth transition to, measurements on the NMR receiver, they do suffer the drawback of a limited dynamic range. Therefore, as shown in fig. 4, the voltage setting of the oscilloscope is optimized. A small voltage scale (vertically zoomed in) maximizes the difference between the amplified noise coming from the receiver chain and the intrinsic noise of the oscilloscope that is seen for frequencies above 35 MHz. However, a voltage scale that is too small results in a time-domain waveform that is (vertically) clipped, leading to a clear distortion of the PSD (shown in blue). In the example of fig. 4, it is clear that a 10 mV choice of voltage scale (gold) shows the expected large (two orders of magnitude) drop in the PSD at the filter cutoff while still avoiding the clipping-induced distortion seen at 5 mV (blue). (Note that fig. 4 represents a relatively high-noise configuration in order to emphasize this dynamic range optimization).

Fig. 4 demonstrates that even after averaging the PSD from 100 captures (possible in under three minutes) to yield the faint, more transparent lines, these lines still appear broad/thick due to rapid frequency-dependent oscillations in the noise. Convolution with a gaussian filter of sufficient width (here 100 kHz; the more intense lines of matching color) smooths the noise PSD sufficiently to identify key features, and also allows interpretation of a PSD subjected to minimal (or no) signal averaging.

III.4. Generation of Test Signal

A variety of sources can generate a test signal at a fixed voltage and frequency (the results here employ the previously mentioned programmable AFG). However, testing with the duplexer in place requires signal at the level of NMR signal—at the μV to nV level. Therefore, it becomes necessary to connect precisely calibrated attenuators to the output of the frequency source. This is achieved by designating “attenuator assemblies:” the combination of an attenuator with attached cabling and/or adapters that begins with a BNC jack (F) and ends with a BNC plug

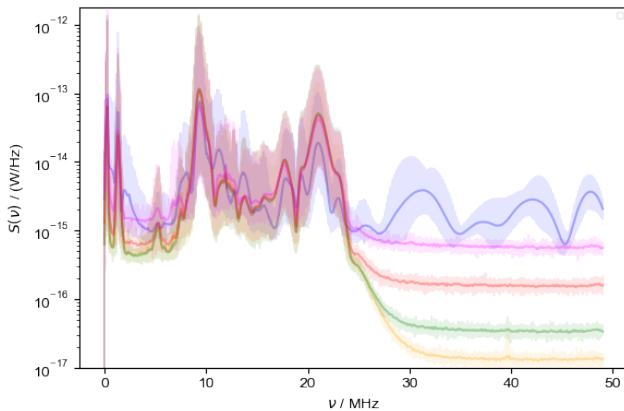


FIG. 4. An oscilloscope set to a sampling rate of 100 MSPS and a voltage scale of 5 (blue), 10 (gold), 20 (green), 50 (red) and 100 mV (magenta), digitized 100 traces of noise acquired from the output end of the receiver chain (fig. 3). In each case, a 100 kHz Gaussian convolution generates the more intense line from the data shown with the more transparent line of the same color.

(M). With the frequency source set to a high voltage, an oscilloscope measures the output of each such assembly to allow calculation of the attenuation. (With care to remember the unusual rules for significant figures of logarithmic quantities.) The measurement is repeated several times, to check for variations due to cable positioning.

To generate the test signal, the frequency source is set to a mV-level voltage (and measured on the oscilloscope), and several attenuator assemblies can then be connected as needed, without the insertion losses from any intervening cabling. In order to speed this calibration, a simple script captures the oscilloscope data and automatically converts to analytic signal, filters, and measures the rf voltage amplitude.

To generate the test signal, the frequency source is set to a mV-level voltage (and measured on the oscilloscope), and several attenuator assemblies can then be connected as needed, without the insertion losses from any intervening cabling. A simple script to capture the oscilloscope data to automatically convert to analytic signal, filter, and measure the rf voltage can speed this process.

III.5. Further Details

The test signal is used in quantifying the gain of the receiving pathway (sec. S2.4), as well as a on-resonance calculation of the transceiver input calibration factor (sec. S2.1). Further, the GDS captures the output pulse in calculating the $t_{90}\sqrt{P_{tx}}$ (sec. S2.5).

When attenuating down the high frequency noise (sec. S2.2), a variable attenuator (KAY electronics) with 3 dB, 10 dB, 13 dB, 23 dB and 50 dB is placed between the output of the receiver chain and the input of the SpinCore transceiver board.

IV. Results and Discussion

The principal result presented here is a protocol that enables detailed characterization and optimization of the absolute signal and noise levels. The sections below, in order, outline an example of such a protocol, with various technical details supported by the methods section and the SI (referenced as relevant). Over the course of this protocol, the validity and utility of the reorganized theory (presented above) are also explored, as well as various specific observations pertaining to the low-field ODNP system investigated here.

IV.1. Noise PSDs from Test and Measurement Equipment

A single unprocessed capture of the noise on the NMR receiver or an oscilloscope yields a relatively uninformative picture, allowing calculation of the standard deviation of the noise voltage and little else [18, 22]. Spectrum analyzers can quantify noise with a high dynamic range, and prove particularly useful for LNA noise factor quantification, while VNAs can identify cross-talk between components (S_{12}) [20, 48–50]. However, both for limiting the necessary additional instrumentation, and for easier comparison to the NMR transceiver, the protocol here relies primarily on a standard digital oscilloscope to capture the noise that is output by the receiver chain. Eq. 16 then converts the captured time-domain traces to PSDs.

IV.1.A. Intrinsic Noise of the Receiver Chain

The green line in fig. 5 shows the thermal noise limit for the (previously described) receiver chain. Specifically it corresponds to the gain of the receiver chain (measured in sec. S2.4, fig. S4) multiplied by the theoretical Johnson-Nyquist noise (eq. 11).

With a 50 Ω terminator attached to its input, the (shielded) receiver chain emits the noise density shown in magenta. The shape and amplitude of this line match expectations based on the measured gain of the receiver chain. In particular, there is a noise cutoff at 26 MHz due to the presence of the low pass filter at the end of the receiver chain, the 1/f noise of the LNAs is clearly identifiable at frequencies below 1 MHz, and at intervening frequencies, the noise density appears approximately flat. The fact that the measured noise *vs.* the thermal noise limit are separated by a factor of 2, and only for a limited range around the intended resonance frequency of 14–15 MHz, is expected here. This is because the duplexer contains various frequency-sensitive components that filter signal outside the 14–15 MHz range to varying extents, while the LNAs are broadband and will continue to transmit a noise level appropriate for their noise figure (which is specified as 2.9 dB).

Fig. 5 also highlights a major unexpected issue: attaching the NMR probe to the receiver chain introduces interference noise (EMI) that exceeds the thermal noise limit by two orders of magnitude. Such high levels of EMI prevent the isolation of small amounts of signal–

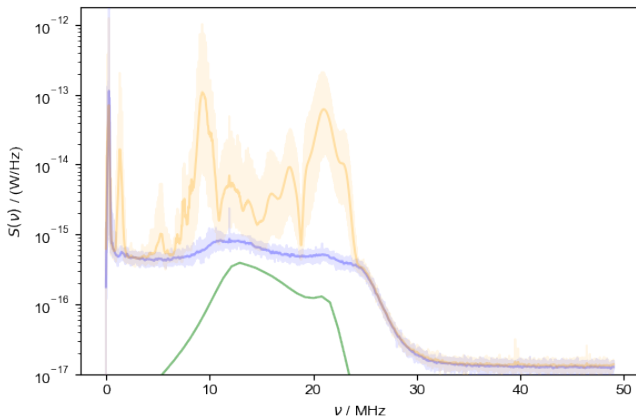


FIG. 5. The noise PSD of the terminated receiver pathway (blue) rises slightly above the thermal noise limit (green) over the sensitive range of the spectrometer (14-15 MHz). The shape of the thermal noise limit is controlled by the gain of the receiver chain (fig. S4), which is non-uniform here. When the NMR probe is attached to the input of the receiver pathway (gold), very strong EMI appears.

especially when considering, *e.g.*, the un-enhanced reference scan for an ODNP experiment, which comes from a 3.5 μL sample with only thermal (Boltzmann) levels of spin polarization. However, as will be demonstrated, the distinctive shape (fingerprint) and frequency specificity of this measurement allows the spectroscopist to systematically identify and mitigate the source of the EMI.

Note that frequency-domain convolution (eq. 16) of the noise PSD proves crucial to developing clear results for this section. As noted in the methods section, the apparent broadness of the un-convolved data (the more transparent line) arises from high-resolution oscillations. These oscillations make it difficult to extract identifying details like the $1/f$ noise or distinctive frequency variations arising from particular sources of EMI. The origins of these oscillations will be interpreted later; at this stage in the protocol, however, simply note that an empirical observation of the line “thickness” drives the choice of convolution width in eq. 16 (here $\sigma = 100\text{kHz}$).

IV.1.B. Example: Investigating Source of Noise

ODNP spectroscopists are relatively familiar with the fact that a commercial electromagnet power supply can emit large amounts of EMI[6, 31]. The noise PSD measurement protocol allows almost any lab to measure and confirm the nature of this noise (here from the Bruker E500 system, fig. 6).

Fig. 6 shows that the electromagnet power supply introduces EMI that travels through free space and that is approximately two orders of magnitude greater than standard thermal (Johnson) noise. Specifically, the act of turning on the electromagnet power supply introduces the overwhelming majority of the noise (gold \rightarrow green). Removing the probe from the cavity and placing it on a nearby table breaks any potential direct current path be-

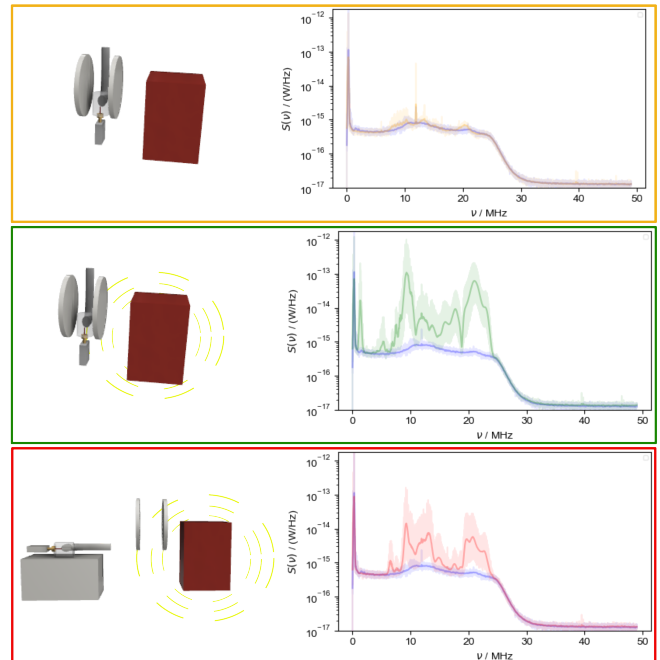


FIG. 6. The noise PSD levels of a terminated BNC cable connected to the input of the receiver chain (blue line) provides a baseline reference for all plots. All other lines show the noise output by the receiver chain when connected to the NMR probe (grounded to the ESR cavity for gold and green). When the power supply is off (gold), the noise density closely approaches the noise levels of the terminated receiver chain (blue). Turning on the electromagnet power supply introduces dramatic noise (green). Disconnecting the probe from the cavity, and placing it on a table 5 ft from the power supply causes subtle changes to the data (red), as discussed in the text.

tween the probe and the ESR power supply. One would expect that this action would remove any noise brought on by spurious electrical connections, ground loops, *etc.* However, it yields only a slight decrease of the noise and a redistribution in frequency space. Thus, the test of fig. 6 leaves the only likely transmission path between the power supply and the probe to be through-space EMI.

Notably the type of variation in frequency distribution seen between the green and red curves occurs not only with movement of equipment, but also simply over longer periods of time. Therefore this measurement underscores an important point about the noise measurement protocol: It is important to look at the PSD over a broad frequency range. Exclusively observing noise densities zoomed in to more specific frequency ranges could make it appear that the noise was increasing or decreasing when various changes are made when, on average, it is not.

Note that, in order to give an example of the protocol advocated here, the subsequent subsections illustrate two well-reasoned steps towards improving the noise that do not yield a significant effect before exploring one that does. It’s important to note that none of these steps

is, in itself overly dramatic or original. Rather, the resulting demonstration shows how a reasonably processed broadband noise PSD can systematically select between different noise mitigation options.

IV.1.C. Test 1: Analysis of Shielding

An implied advantage of the design adapted from Kaminker [29] is that the grounded elements of the probe (especially the coil) and cavity would together form a Faraday cage that would shield the probe from EMI. The fact that removing the probe from the cavity and exposing it to the environment (green \rightarrow red in fig. 6) results in reduced noise is thus surprising.

Therefore, a series of measurements tested the integrity of the shielding scheme. Three noise PSDs were acquired: one with the NMR probe secured and properly grounded to the cavity, a second where the cavity/probe/waveguide assembly is detached from the ESR microwave bridge and simply held between the magnets, and a third where the probe is completely disconnected from the cavity held between the magnets plates (fig. 7). The lack of a dramatic change in the overall noise density indicates that the cavity likely provides insufficient shielding for the NMR probe.

Thus, fig. 7 identified that basic steps towards improving the shielding might prove an effective strategy for noise mitigation. First, optimization of connections between NMR probe and cavity—including improving the metal-to-metal contact between various parts and adding conducting foil over joints—yielded no improvement (not shown). Also, insertion of a copper plate into the waveguide connection in an attempt to improve the grounding between the NMR probe and the cavity/waveguide assembly (a strategy that was shown to work well in the Han lab [7]), demonstrated no improvement (not shown). Finally, while a secondary shielding enclosure may still prove successful for mitigating this noise, this was beyond the scope of basic improvements, and, as shown in subsequent subsections, proved unnecessary.

IV.1.D. Test 2: Balanced Probe Design

A balanced probe design (green circuit in fig. 8) aims to concentrate the current within the circuit near the coil and to mitigate the antenna effect by approximately equalizing the impedance to ground on either end of the coil [51, 52]. Here, the standard tank circuit (gold circuit in fig. 8) is referred to as the “single-sided tank probe” for contrast. Both coils have a sample volume of 8.6 μ L, utilize a double hairpin loop, and integrate specifically into a Bruker Super High Sensitivity Probehead X-Band resonator (ER 4122 SHQE). In addition to the circuitry, the two probes differ in shielding: a thicker 6.5 mm aluminum box encases the single-sided tank probe while a 1.5 mm thick aluminum box encases the balanced probe. When the single-sided tank probe is connected in place of the balanced probe, the receiver picks up slightly less interference noise, as shown in fig. 8. This measurement emphasizes that the interference noise transmitted by the power supply here does not interact solely with the coil;

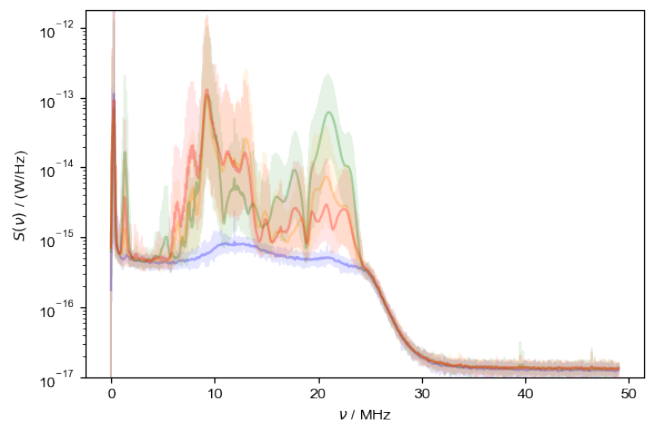


FIG. 7. Various noise measurements acquired to check the integrity of the cavity/probe shielding. As seen repeatedly, in the standard configuration (green – same as green in fig. 6), large spikes appear. By detaching the waveguide/bridge connection (gold) the noise at frequencies higher than 13 MHz drop an order of magnitude, but lower frequencies increase slightly. Entirely detaching the tuning box from the cavity (red) and holding it between the magnets does not yield dramatic changes in the noise density. (Terminated receiver chain noise shown in blue for reference.)

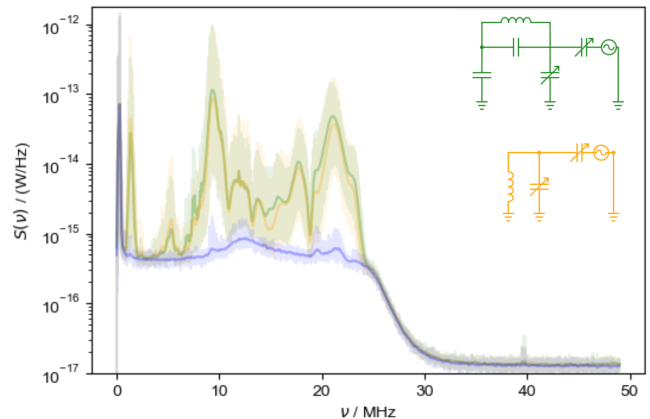


FIG. 8. Different probe circuitry doesn’t aid in preventing EMI pickup. When the DC supply of the Bruker E500 is powered on, the resulting interference noise transmits slightly more efficiently into the balanced NMR probe (green) vs the single-sided tank probe (gold). Also includes reference baseline of terminated receiver chain (blue).

rather, it interacts with the probe and ESR cavity assembly as a whole. The slight differences (fig. S5) between the two probes may arise either from the thicker shielding of the single-sided tank probe, or from incidental changes to the rf cross-section of the probe.

IV.1.E. Test 3: rf Chokes Mitigate Electromagnetic Interference

Ferrite chokes are a common solution for mitigating high-frequency EMI by selectively increasing the impedance of common mode transmission while leaving

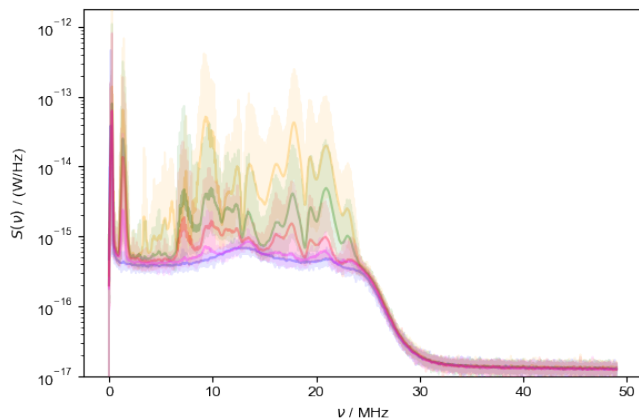


FIG. 9. Common-mode chokes do mitigate the EMI, as illustrated by the noise PSD from the standard configuration (equivalent to green of fig. 6) with 0 (gold), 6 (green), 12 (red) and 26 (magenta) ferrite bead chokes added to the coaxial cable connecting the probe to the receiver chain. (Baseline noise of terminated receiver chain shown in blue.)

the impedance of the transverse (TEM) mode unaltered. Fig. 9 shows how progressive addition of snap-on chokes to the coaxial cable connecting the probe to the receiver chain progressively mitigates the EMI.

IV.2. Noise PSDs Acquired by NMR Transceiver

There is little quantitative value to the broadband noise PSD measurements unless they correspond to the noise actually digitized on the NMR receiver (transceiver). Therefore, the protocol advocated here next quantifies the noise density on the receiver and compares it to the broadband oscilloscope[?] measurements.

IV.2.A. Receiver calibration factor

Receivers frequently collect and present acquired data with arbitrary units intrinsic to the board. For example, the SpinCore RadioProcessorG transceiver used in this example acquires NMR signal as an integer on a $0 \rightarrow 2^{14}$ scale.[53] This introduces a need for a receiver calibration factor to convert the intrinsic transceiver board digital units (abbreviated as “dg”) to standard units such as voltage. Initial calibration of the receiver calibration factor was performed by outputting ≈ 10 mV (exact value verified by oscilloscope capture), close to the transceiver carrier frequency (*cf.* eq. 15), directly to the input of the SpinCore transceiver board (tbl. I), and fitting the acquired time domain signal to a complex exponential with constant magnitude in order to obtain the amplitude in [dg], which is compared to the amplitude in [V] of the same signal when measured on an oscilloscope. For the widest spectral width (75 MHz, the base digitizer frequency), a calibration factor of 6.0 dg/ μ V was measured.

IV.2.B. Comparison of Oscilloscope vs Transceiver Noise Measurements

The noise PSD of the terminated receiver chain is acquired on the transceiver board at the maximal digitiz-

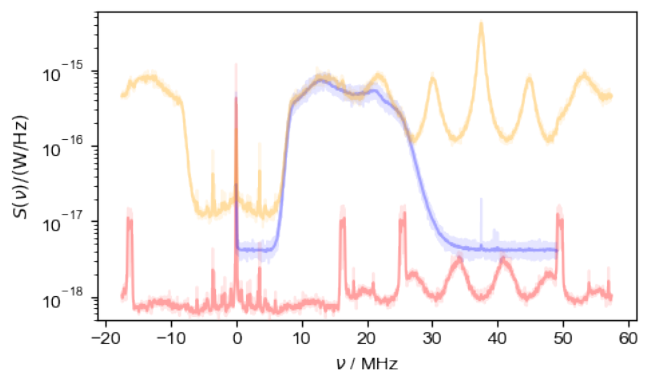
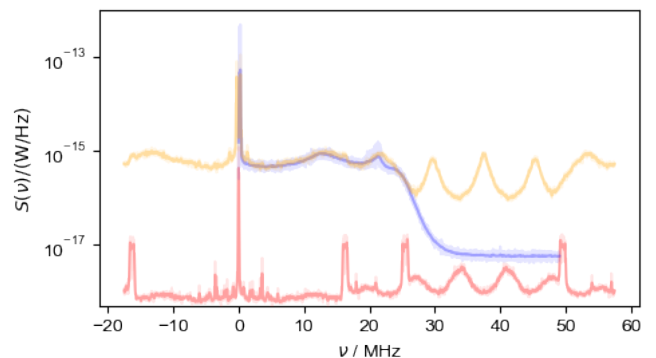


FIG. 10. A) The PSD of the terminated receiving chain is acquired on the oscilloscope (blue) as well as on the transceiver board with a carrier frequency of 20 MHz and a spectral width of 75 MHz (gold). The noise PSD of the terminated SpinCore (red) shows the intrinsic noise of the transceiver board itself. B) A high pass filter is placed at the output of the low pass filter and the PSD is acquired again both on the oscilloscope and the transceiver board (plotted with the same color scheme as A).

ing rate (75 MHz) and compared to the PSD acquired on the oscilloscope (fig. 10). Specifically, the SpinCore API Python extension [47] captures a time-domain trace using the same functions that are employed for NMR signal acquisition, and division by the calibration factor [dg/V] appropriately converts the units to volts. Subsequently, just as for oscilloscope captures, eq. 16 converts the time-domain data to a PSD.



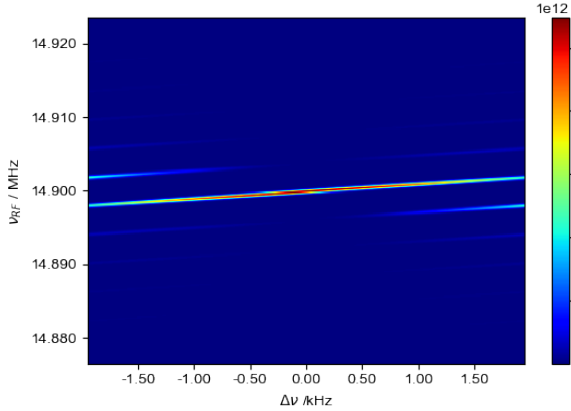
Over frequencies less than ≈ 18 MHz, when digitizing the noise from the terminated receiver chain, the transceiver observes a similar noise density as the oscilloscope measurements. However, the noise PSD of the terminated receiver chain, as acquired on the transceiver board, differs drastically from the PSD acquired on the oscilloscope at frequencies higher than 20 MHz. Specifically, peaks with a noise density similar to or greater than the noise coming from the receiver chain appear at frequencies ≥ 26 MHz, where the receiver chain does not transmit any noise, while for frequencies slightly higher than 20 MHz, the transceiver introduces noise that overlaps with the noise transmitted from the receiver chain. Notably, the transceiver only develops these contribu-

tions in response to a significant power density of noise— with a terminated transceiver input, the noise density drops several orders of magnitude and change in frequency (fig. ??, red) As noted in the SI (fig. S2), these high-frequency noise peaks do scale roughly linearly with the input. Therefore, one can suggest that they arise from accidental mixing of the actual input with internal clock signals, *etc.* Interestingly, as shown in fig. 10, addition of a high pass filter does mitigate low-frequency noise, but actually exacerbates the contribution of these internally-generated high-frequency peaks. Fortunately, the applications here require only 12-16 MHz carrier frequencies; therefore, if the high-frequency peaks can be digitally filtered, they are not of concern here.

IV.2.C. Testing Oversampling Performance

Smaller spectral widths yield higher resolution and allow more insight to the noise present at spectral widths that are more typical for an NMR experiment.

By varying the frequency of a ≈ 10 mV test signal, directly injected into the transceiver, and maintaining the carrier frequency, the digital filter of the transceiver board can be traced by plotting the amplitudes of PSD at each rf frequency (fig. 11).



The 2D image (fig. ??), is an excellent illustration of the aliasing that occurs as the signal drifts off resonance with the carrier while the 1D plot of the PSD amplitudes clearly shows a good fit to the absolute of a sinc function. A sinc function in the frequency domain translates to the digitizer applying box-car averaging rather than a FIR filter upon acquisition. As a consequence, the filter function became a necessary component in processing the data acquired on the transceiver board.

This test is further extended to larger spectral width in order to calculate the receiver calibration factor (fig. ??)

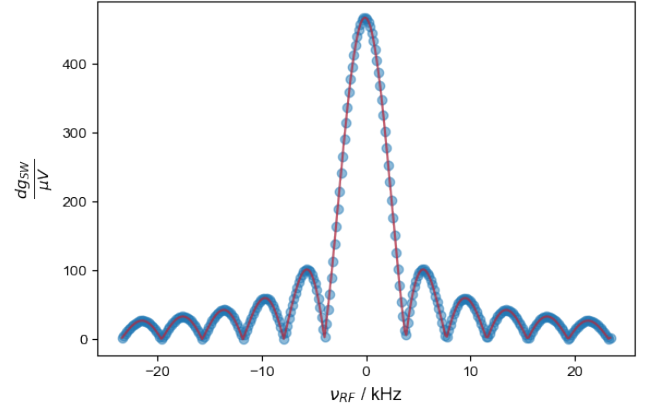
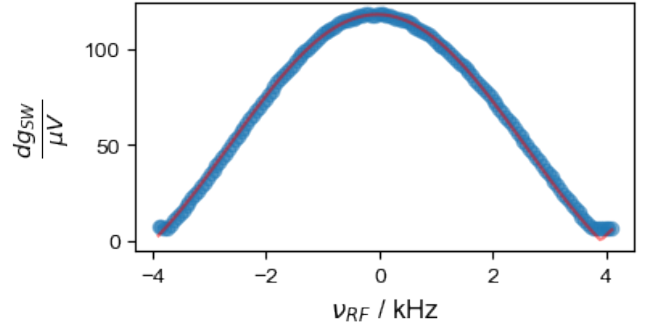
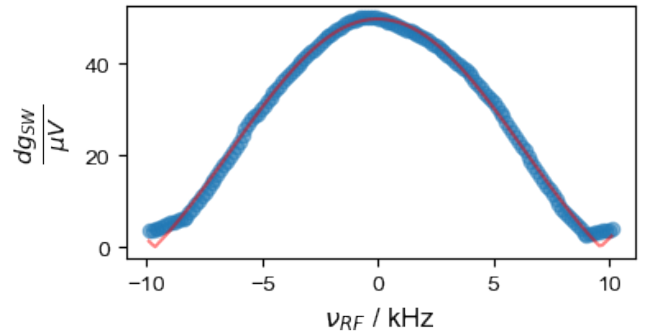


FIG. 11. Test signal outputs measured test signal at frequencies ranging from 14.8766 MHz to 14.9234 MHz and is collected on the SpinCore with a carrier frequency of 14.9 MHz. Top) A 2D plot shows the intensity of the PSD acquired at each output frequency (ν_{RF}). Bottom) The maximum for the PSD for each output frequency is plotted as a function of the offset from 14.9 MHz. A absolute of a sinc function perfectly fits with the plotted data.



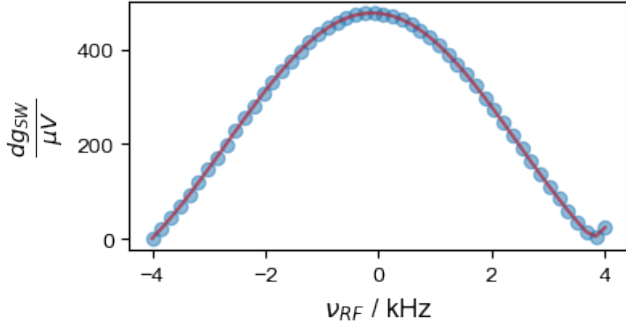
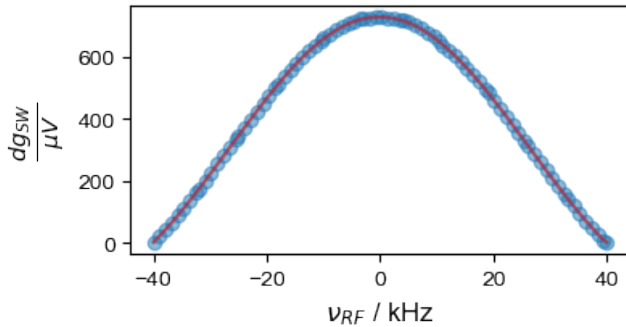
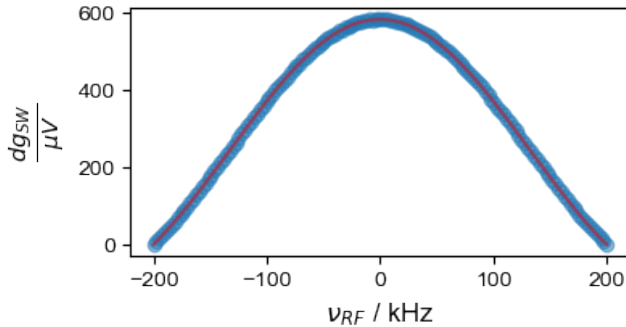
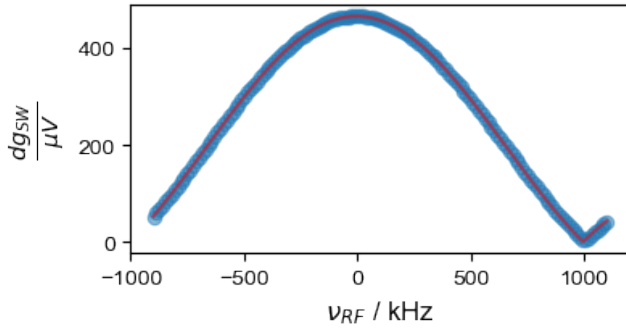
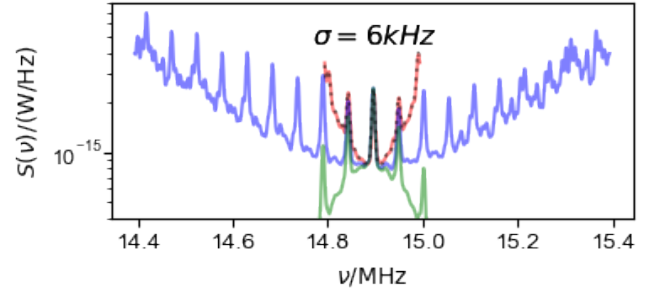
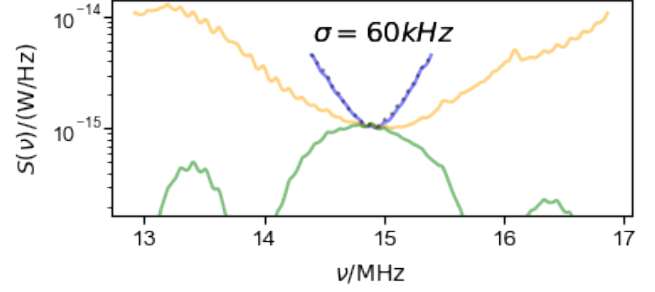


FIG. 12. Test signal is output at varying frequencies from the AFG and acquired at a carrier frequency of 14.9 MHz on the SpinCore receiver board. The maximum of the resulting PSD for each output frequency is plotted as a function of the offset and divided by the actual value of the test signal. The transceiver response is plotted for A) 3.9 kHz, B) 40 kHz, C) 200 kHz, D) 1 MHz, E) 4 MHz, and F) 10 MHz.



The traced digital filters at larger spectral widths demonstrate a decent fit to the absolute of a sinc func-

tion at the kHz scale of spectral widths but the fits start to deviate slightly at MHz spectral widths due to the inhomogeneity of the gain of the receiver chain.



As illustrated in fig. 13, oversampling allows the digitization of more noise energy over a smaller bandwidth thus a smaller convolution filter width is needed to resolve the noise PSD. At spectral widths smaller than 1 MHz periodic spikes in the noise PSD appear that match the periodic peaks captured in the time domain on the oscilloscope indicating the electromagnetic noise emitted by the power supply is indeed time periodic(fig. 13).

This process is continued, decreasing the spectral width incrementally until the spectral width at which a typical NMR spectra would actually be acquired (fig. 14)

Although there is aliasing present it is clear that the spectra nearest the carrier do indeed match thus validating the receiver calibration coefficients as well as our understanding of the response of the transceiver board.

IV.2.D. Noise PSDs at Different SW

With the response of the transceiver board fully characterized, predicting the noise PSD acquired on the transceiver board then becomes a simple step by step process:

1. Convert the larger spectral width data to Volts and calculate the PSD
2. Divide by the digital filter specific to the larger spectral width (ex. gold line in A of fig. 13).
3. Apply the digital filter for the smaller, desired spectral width (ex. green line in fig. 13).
4. Down sample the time domain spline of the larger spectral width using the spacing of points in the smaller spectral width dataset (ex. blue line in A of fig. 13). Using this simple method, the PSD of decreasing spectral widths can be accurately predicted as shown by fig. 13.

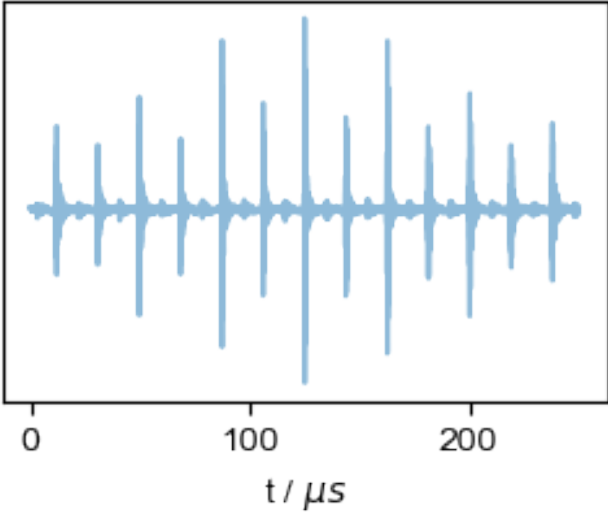


FIG. 13. A) The measured noise PSD for a dataset with a spectral width of 4 MHz is divided by the sinc filter appropriate for a spectral width of 4 MHz resulting in the gold line, and subsequently multiplied by a sinc function appropriate for a spectral width of 1 MHz resulting in the green line. The prediction (dashed black line) for the noise PSD for a dataset with a spectral width of 1 MHz (blue) matches well with the actual noise PSD. The convolution filter at this range of spectral widths is 60 kHz and forms a fairly smooth dip. B) The measured noise PSD for a dataset with a spectral width of 1 MHz is divided by a sinc filter appropriate for a spectral width of 1 MHz (blue) and then multiplied by a sinc function appropriate for a dataset with a spectral width of 200 kHz (green). The prediction (dashed black line) for the noise PSD for a dataset with a spectral width of 200 kHz (red) matches well with the actual noise PSD. The convolution filter at this range of spectral widths is 6 kHz and forms periodic spikes. C) The noise in the time domain as acquired on the oscilloscope shows periodic spikes along the time domain corresponding to spikes with a spacing that matches those seen in the frequency domain for higher resolved datasets (<1 MHz).

IV.2.E. Mitigation of Noise as seen on the transceiver

As shown in fig. ??, at higher resolution, the seemingly flat noise PSD is actually a series of noise spikes evenly distributed in the frequency domain. Therefore it is expected that with the addition of the same chokes used in fig. 9, the noise will be fully reduced to the noise of the terminated receiver chain.

Whereas fig. 9 showed a fairly large improvement to the noise between the addition of 12 and 26 chokes, fig. 15 demonstrates that at the spectral widths that are more common to NMR experiments, the transition from 12 to 27 chokes does not have a significant impact. Furthermore, it is illustrated that while the noise spikes evenly along the frequency axis, the frequency range specific to the lab (around 14.89 MHz) falls within one of the dips in the captured noise PSD of fig. 15. Though as stressed previously, the interference noise has been noted to move

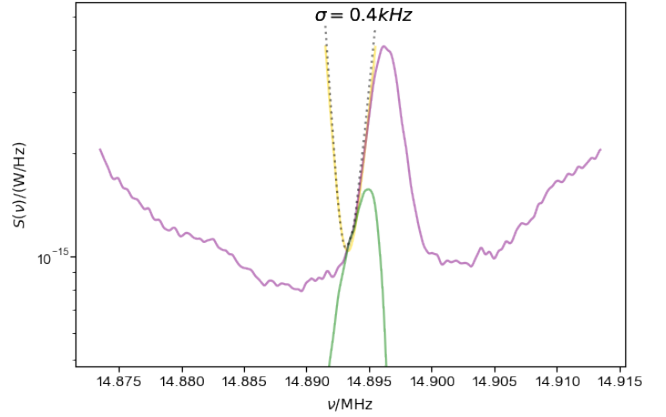


FIG. 14. The PSD acquired on the transceiver board using a spectral width of 40 kHz is divided by a sinc function specific to a spectral width of 40 kHz (purple) and subsequently multiplied by a narrower sinc function appropriate for a dataset with a spectral width of 4 kHz to yield a filtered noise PSD (green). This product was then downsampled to produce the predicted noise PSD for a spectrum taken with a spectral width of 4 kHz (dashed black line). The actual acquired spectra (gold) having a spectral width of 4 kHz shows the exact same PSD as the predicted model.

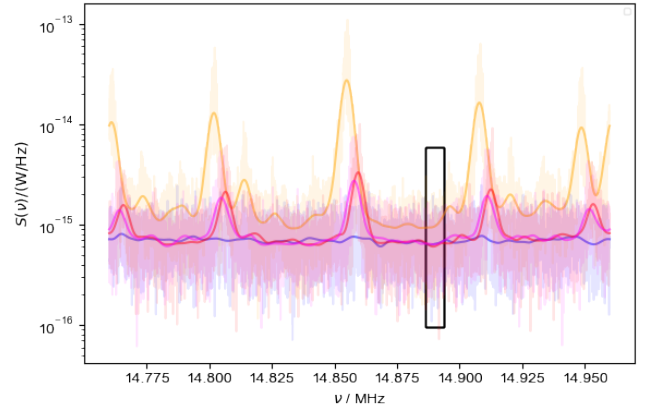


FIG. 15. The noise PSD was acquired at a spectral width of 200 kHz and convolved using a convolution width of 4 kHz. The blue line illustrates the Johnson noise of the terminated receiver chain. Similar to fig. 9, gold shows the PSD for the probe inserted into the cavity with the magnet on, and it is clear that magnitudes of noise are introduced. When 12 chokes are added (red) the noise is halved. The addition of 27 chokes (magenta) results in a very minimal decrease in noise compared to the 12 chokes. A black box encompasses the frequency range used for NMR experiments in the current lab.

throughout the day and therefore the value in acquiring at broader spectral widths serves a great value in optimizing both the noise intensity as well as location of the carrier with respect to the interference noise spikes.

Importantly, the addition of chokes does not affect the

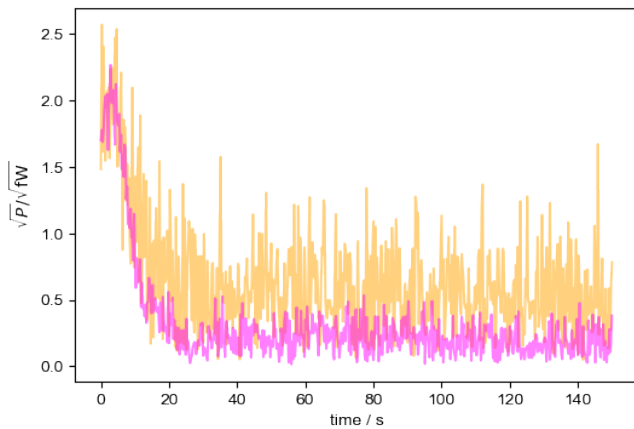


FIG. 16. Data acquired for a TEMPOL sample at a spectral width of 3.9 kHz with (magenta) and without chokes present (gold). Without chokes the noise PSD corresponds to the gold lines in fig. 9, whereas when the chokes are added, the noise PSD is that of the magenta lines in fig. 9.

overall amplitude of signal acquired on the transceiver board and strictly acts in reducing noise alone thus improving the overall SNR(fig. 16).

IV.3. Absolute signal intensity matches prediction

To predict the absolute signal intensity for a tested sample (e.g., 27 mM aqueous TEMPOL), the volume and conversion factor, Λ must be known. To collect the $t_{90}\sqrt{P_{tx,rms}}$ value, a mutation experiment was performed to find the optimal $t_{90} = 4.52\mu s$. Due to pulse rise time imperfections the shape of the pulses are not perfectly square. Significant imperfections in the pulse shape could affect the effective tip angle (though these are not expected to affect the excitation profile) over a frequency range captured via the oscilloscope to yield a total $t_{90}\sqrt{P_{tx,rms}} = 39.4 \mu s\sqrt{W}$ (sec. S2).

These measured values correspond to a conversion factor, Λ , of $1.488 \times 10^{-4}T/\sqrt{W}$ using eq. 2. eq. 5 inputs the measured conversion factor to yield an expected maximum input referred power of $2.38\sqrt{fW}$ for the signal prior to amplification.

A series of echoes with varying lengths between the 90 and 180 pulse were acquired and show an absolute signal with a max that matches well with the predicted value(fig. 17).

Thus, a simple measure of the ninety time, and power of the output pulse can determine the signal levels fairly accurately. This validates application of eq. 10 to determine the field distribution factor (see Theory section for a detailed explanation of the field distribution factor and its close relationship to the filling factor and other historical measures of pulse performance.) After (short-open-load) calibration, the nanoVNA (inexpensive pocket-sized VNA) measures the Q -factor of the probe to be 23.5. From this value, and the previously mentioned value of Λ , eq. 10 determines a field distribution factor

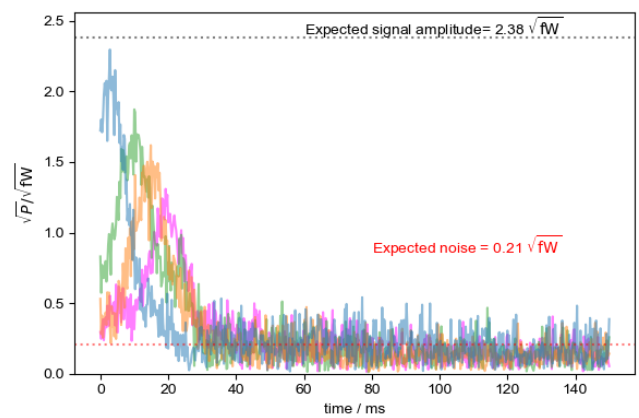


FIG. 17. A varied tau experiment was performed using the same 27 mM TEMPOL sample and a ninety time of $4.52 \mu s$. A dashed black horizontal line indicates the predicted signal amplitude of $2.38 \sqrt{fW}$ while a second red dashed line indicates the expected noise level given the gain and noise figure of the LNAs within the receiver chain enclosure ($0.81 \sqrt{fW}$). The peaks of the varied tau extrapolate to a value that matches the expected signal amplitude of $2.38 \sqrt{fW}$.

of $\eta' = 0.67$. Note that because eq. 10 does not rely on approximations, only physical constants and the values of Q , Λ , and the resonance frequency (also measured, 14.89 MHz), this value of η' can be regarded as a measured value (*vs* an approximation or theoretical calculation.) One could calculate a traditional filling factor here as high as $\eta = 1.0$ (the fraction of the sample volume to the internal volume of the hairpin loop)[(author?) [37]][34]. Thus, result of $\eta' = 0.67$ is surprisingly low, indicating that of the energy that it stores in a resonance cycle, the resonator directs only 67% towards providing the spins with an rf magnetic field. The rest goes towards the stray magnetic field of the hairpin loop, and likely towards stray inductances inside the tuning circuitry itself (e.g. the inductance of the unmatched coaxial line needed to connect the hairpin loop inside the cavity with the tuning circuitry outside, or straight-wire inductances within the tuning box[34, 37].)

V. Conclusion

The noise and absolute amplitude of signal is easily quantifiable and this paper demonstrates they are easily obtainable using off-the-shelf components. Convolution combined with signal averaging yields incredibly detailed noise PSDs that have yet to be seen in the literature. Integrating a commercial electromagnet into an NMR setup introduces ODNP abilities as well as accommodating interference noise that is easily mitigated through snap-on ferrite chokes. The SNR of acquired NMR signal is greatly improved by the mitigation of noise levels. Combining the concept of reciprocity and the ESR concepts of the conversion factor and the treatment of field distribution results in an accurate estimation of the absolute signal amplitude for NMR signal for a particular lab setup.

These simple measurements greatly improve the ease of integrating modern, new instrumentation for improved, and novel experimentation in both established and newer laboratories alike.

Literature has forewarned the complications that apodization introduces to integral and propagated error calculations in the spectral domain. Calculating these in the time domain as shown in this paper, proves facile, straightforward and accurately determines the integrated signal with propagated error. This proves a great advantage as it still permits the use of apodization to any degree but sidesteps the complications of calculations in the frequency domain. This method can thus be used to simplify and more accurately present quantitative NMR results.

checks

- do we point out that broadband noise PSD is even

applicable when there is slow frequency variation of the EMI?

- “An open-source software toolkit that controls a standard AFG and digitizes on a standard oscilloscope accompanies this paper, **with examples provided corresponding to each of the figures.**”
- AG updates most recent version of notebook, and JF confirms relation between prediction and measurement.
- Decide on feasibility of this:

In the specific context of ODNP, we show that this protocol makes it possible to measure the enhancements arising from very low concentrations of spin label on a hardware system where this would not otherwise be possible.

-
- [1] T. Maly, G. T. Debelouchina, V. S. Bajaj, K.-N. Hu, C.-G. Joo, M. L. Mak–Jurkauskas, J. R. Sirigiri, p. d. u. family=Wel, given=Patrick C. A., J. Herzfeld, R. J. Temkin, and R. G. Griffin. “Dynamic nuclear polarization at high magnetic fields.” 128(5):052211. doi:10.1063/1.2833582.
- [2] A. N. Smith, M. A. Caporini, G. E. Fanucci, and J. R. Long. “A Method for Dynamic Nuclear Polarization Enhancement of Membrane Proteins.” 127(5):1562–1566. doi:10.1002/ange.201410249.
- [3] B. S. Marques, M. A. Stetz, C. Jorge, K. G. Valentine, A. J. Wand, and N. V. Nucci. “Protein conformational entropy is not slaved to water.” 10(1):17587. doi:10.1038/s41598-020-74382-5.
- [4] A. Dey and A. Banerjee. “Unusual Overhauser Dynamic Nuclear Polarization Behavior of Fluorinated Alcohols at Room Temperature.” 123(49):10463–10469. doi:10.1021/acs.jpcc.9b08144.
- [5] A. A. Beaton, A. Guhness, and J. M. Franck. “A modernized view of coherence pathways applied to magnetic resonance experiments in unstable, inhomogeneous fields.” 157(17):174204. doi:10.1063/5.0105388.
- [6] J. M. Franck and S. Han. “Overhauser Dynamic Nuclear Polarization for the Study of Hydration Dynamics, Explained.” In “Methods in Enzymology,” volume 615, pages 131–175. Elsevier. ISBN 978-0-12-816762-5.
- [7] J. M. Franck, A. Pavlova, J. A. Scott, and S. Han. “Quantitative cw Overhauser effect dynamic nuclear polarization for the analysis of local water dynamics.” 74:33–56. doi:10.1016/j.pnmrs.2013.06.001.
- [8] A. E. Marble, I. V. Mastikhin, B. G. Colpitts, and B. J. Balcom. “A compact permanent magnet array with a remote homogeneous field.” 186(1):100–104. doi:10.1016/j.jmr.2007.01.020.
- [9] T. Kremer, T. Irons, M. Müller-Petke, and J. Juul Larsen. “Review of Acquisition and Signal Processing Methods for Electromagnetic Noise Reduction and Retrieval of Surface Nuclear Magnetic Resonance Parameters.” 43(4):999–1053. doi:10.1007/s10712-022-09695-3.
- [10] R. Kleinberg. “NMR well logging at Schlumberger.” 13:396–403. doi:10.1002/cmr.1026.
- [11] G. Jin, R. Xie, and B. Jin. “New Insight Into Data Processing of Nuclear Magnetic Resonance Logging for Pore Structure Characterization in Tight Sandstone Reservoirs.” 62:1–10. doi:10.1109/TGRS.2024.3368096.
- [12] T. Lin, Y. Zhang, and M. Muller-Petke. “Random Noise Suppression of Magnetic Resonance Sounding Oscillating Signal by Combining Empirical Mode Decomposition and Time-Frequency Peak Filtering.” 7:79917–79926. doi:10.1109/ACCESS.2019.2923689.
- [13] T. Lin, Y. Yang, F. Teng, and M. Müller-Petke. “Enabling surface nuclear magnetic resonance at high-noise environments using a pre-polarization pulse.” 212(2):1463–1467. doi:10.1093/gji/ggx490.
- [14] B. Blümich and J. Anders. “When the MOUSE leaves the house.” 2(1):149–160. doi:10.5194/mr-2-149-2021.
- [15] T. Hiller, R. Dlugosch, and M. Müller-Petke. “Utilizing pre-polarization to enhance SNMR signals—effect of imperfect switch-off.” 222(2):815–826. doi:10.1093/gji/ggaa216.
- [16] L. Yang, W. He, Y. He, J. Wu, S. Shen, and Z. Xu. “Active EMI Suppression System for a 50 mT Unshielded Portable MRI Scanner.” 69(11):3415–3426. doi:10.1109/TBME.2022.3170450.
- [17] D. D. L. Chung. “Materials for electromagnetic interference shielding.” 255:123587. doi:10.1016/j.matchemphys.2020.123587.
- [18] M. C. Boucher, C. E. Isaac, P. Sun, P. P. Borbat, and J. A. Marohn. “A Non-Perturbative, Low-Noise Surface Coating for Sensitive Force-Gradient Detection of Electron Spin Resonance in Thin Films.” 17(2):1153–1165. doi:10.1021/acsnano.2c08635.
- [19] “Shielding and grounding in large detectors.”
- [20] S. Sankaran, K. Deshmukh, M. B. Ahamed, and S. K. Khadheer Pasha. “Recent advances in electromagnetic interference shielding properties of metal and carbon

- filler reinforced flexible polymer composites: A review.” 114:49–71. doi:10.1016/j.compositesa.2018.08.006.
- [21] T. J. Keller, A. J. Laut, J. Sirigiri, and T. Maly. “High-resolution Overhauser dynamic nuclear polarization enhanced proton NMR spectroscopy at low magnetic fields.” 313:106719. doi:10.1016/j.jmr.2020.106719.
- [22] P. Andris, E. F. Emery, and I. Frollo. “Analysis of NMR Spectrometer Receiver Noise Figure.” 2019:e1083706. doi:10.1155/2019/1083706.
- [23] P. Andris and I. Frollo. “Noise and interference in measured NMR images.” 77:29–33. doi:10.1016/j.measurement.2015.09.003.
- [24] P. Andris, V. Jacko, T. Dermek, and I. Frollo. “Noise measurement of a preamplifier with high input impedance using an NMR console.” 55:408–412. doi:10.1016/j.measurement.2014.05.032.
- [25] M. Goryawala, M. Sullivan, and A. A. Maudsley. “Effects of Apodization Smoothing and Denoising on Spectral Fitting.” 70:108–114. doi:10.1016/j.mri.2020.04.013.
- [26] A. Ebel, W. Dreher, and D. Leibfritz. “Effects of zero-filling and apodization on spectral integrals in discrete Fourier-transform spectroscopy of noisy data.” 182(2):330–338. doi:10.1016/j.jmr.2006.06.026.
- [27] D. D. Traficante and M. Rajabzadeh. “Optimum window function for sensitivity enhancement of NMR signals.” 12(2):83–101. doi:10.1002/(SICI)1099-0534(2000)12:2<83::AID-CMR3>3.0.CO;2-H.
- [28] R. R. Ernst and W. A. Anderson. “Application of Fourier Transform Spectroscopy to Magnetic Resonance.” 37(1):93–102. doi:10.1063/1.1719961.
- [29] I. Kaminker, R. Barnes, and S. Han. “Chapter Sixteen - Overhauser Dynamic Nuclear Polarization Studies on Local Water Dynamics.” In P. Z. Qin and K. Warneke, editors, “Methods in Enzymology,” volume 564 of *Electron Paramagnetic Resonance Investigations of Biological Systems by Using Spin Labels, Spin Probes, and Intrinsic Metal Ions, Part B*, pages 457–483. Academic Press.
- [30] T. Überrück, M. Adams, J. Granwehr, and B. Blümich. “A compact X-Band ODNP spectrometer towards hyperpolarized 1H spectroscopy.” 314:106724. doi:10.1016/j.jmr.2020.106724.
- [31] J.-H. Ardenkjaer-Larsen, G. S. Boebinger, A. Comment, S. Duckett, A. S. Edison, F. Engelke, C. Griesinger, R. G. Griffin, C. Hilty, H. Maeda, G. Parigi, T. Prisner, E. Ravera, p.-u. family=Bentum, given=Jan, S. Vega, A. Webb, C. Luchinat, H. Schwalbe, and L. Frydman. “Facing and Overcoming Sensitivity Challenges in Biomolecular NMR Spectroscopy.” 54(32):9162–9185. doi:10.1002/anie.201410653.
- [32] P. Pham, R. Mandal, C. Qi, and C. Hilty. “Interfacing Liquid State Hyperpolarization Methods with NMR Instrumentation.” 10–11:100052. doi:10.1016/j.jmro.2022.100052.
- [33] “Critical factors in the design of sensitive high resolution nuclear magnetic resonance spectrometers.” 344(1638):311–340. doi:10.1098/rspa.1975.0104.
- [34] D. I. Hoult and R. E. Richards. “The signal-to-noise ratio of the nuclear magnetic resonance experiment.” 24(1):71–85. doi:10.1016/0022-2364(76)90233-X.
- [35] D. J. Jiang and D. R. T. Weber. “Elexsys E 500 User’s Manual: Basic Operations.”
- [36] W. Mims. “Electron Spin Echoes.” In “Electron Paramagnetic Resonance,” pages 263–351.
- [37] G. A. Rinard, R. W. Quine, R. Song, G. R. Eaton, and S. S. Eaton. “Absolute EPR Spin Echo and Noise Intensities.” 140(1):69–83. doi:10.1006/jmre.1999.1823.
- [38] R. R. Mett, J. W. Sidabras, I. S. Golovina, and J. S. Hyde. “Dielectric microwave resonators in TE011 cavities for electron paramagnetic resonance spectroscopy.” 79(9):094702. doi:10.1063/1.2976033.
- [39] R. G. Griffin and T. F. Prisner. “High field dynamic nuclear polarization—the renaissance.”
- [40] V. K. Michaelis, R. G. Griffin, B. Corzilius, and S. Vega. *Handbook of High Field Dynamic Nuclear Polarization*. John Wiley & Sons. ISBN 978-1-119-44169-4.
- [41] F. D. Doty. “Probe Design and Construction.” In “eMagRes,” John Wiley & Sons, Ltd. ISBN 978-0-470-03459-0.
- [42] H. Nyquist. “Thermal Agitation of Electric Charge in Conductors.” 32(1):110–113. doi:10.1103/PhysRev.32.110.
- [43] D. Fitzpatrick. “Chapter 14 - Noise Analysis.” In D. Fitzpatrick, editor, “Analog Design and Simulation Using OrCAD Capture and PSpice (Second Edition),” pages 197–208. Newnes. ISBN 978-0-08-102505-5.
- [44] H. Friis. “Noise Figures of Radio Receivers.” 32(7):419–422. doi:10.1109/JRPROC.1944.232049.
- [45] D. D. Griffin, R. L. Kleinberg, and M. Fukuhara. “Low-frequency NMR spectrometer.” 4(9):968. doi:10.1088/0957-0233/4/9/009.
- [46] C. Motchenbacher and J. Connelly. *Low-Noise Electronic System Design*. Wiley-Interscience.
- [47] J. Franck, A. Beaton, and A. Guinness. “Spincore api python extension.” https://github.com/jmfrancklab/spincore_apps/ (2016).
- [48] D. K. Rytting. “Network Analyzer Accuracy Overview.” In “58th ARFTG Conference Digest,” volume 40, pages 1–13.
- [49] J. A. Nordmeyer-Massner, N. De Zanche, and K. P. Pruessmann. “Noise figure characterization of preamplifiers at NMR frequencies.” 210(1):7–15. doi:10.1016/j.jmr.2011.01.025.
- [50] D. Micheli, R. Pastore, A. Vricella, A. Delfini, M. Marchetti, and F. Santoni. “Chapter 9 - Electromagnetic Characterization of Materials by Vector Network Analyzer Experimental Setup.” In S. Thomas, R. Thomas, A. K. Zachariah, and R. K. Mishra, editors, “Spectroscopic Methods for Nanomaterials Characterization,” Micro and Nano Technologies, pages 195–236. Elsevier. ISBN 978-0-323-46140-5.
- [51] J. Mispelter, M. Lupu, and A. Briguet. *NMR Probeheads for Biophysical and Biomedical Experiments: Theoretical Principles and Practical Guidelines (With CD-ROM)*. PUBLISHED BY IMPERIAL COLLEGE PRESS AND DISTRIBUTED BY WORLD SCIENTIFIC PUBLISHING CO. ISBN 978-1-86094-637-0 978-1-86094-902-9.
- [52] J. Stringer and B. F. Collins. “(54) BALANCED MODE OPERATION OF A HIGH FREQUENCY NMR PROBE.”
- [53] “RadioProcessor-G - SpinCore Technologies.”

Supplemental Materials for: Separate and Detailed Treatment of Absolute Signal and Noise Enables NMR Under Adverse Circumstances

S1. Supplementary information

S1.0.A. Broadband Noise PSD Summary

The problem of DC power supplies acting as noise source for ODNP is not a new observation, and various individual solutions have been implemented, frequently at the expense of great experimental time, but the same solutions do not apply to every unique setup in each laboratory.[?] The overarching observation here is that performing a noise PSD measurement of reasonable quality allows one to: (1) identify primary sources of noise (2) systematically identify which solutions help to mitigate those noise sources, and which do not and (3) identify how closely a particular noise density comes to the idealized thermal (Johnson-Nyquist) noise limit (*vs.* how much interference noise or poor noise figures dominate the noise spectrum.)

Importantly, the measured noised PSDs are expected to be idiosyncratic for the particular laboratory setup where these measurements were acquired; it is the measurement protocol itself rather than the particular data that is expected to prove transferable to other laboratories and types of experiments.

S2. Supporting Information

S2.1. Receiver Calibration Factor

TABLE I: The appropriate receiver calibration factor in units of $\text{dg}/\mu\text{V}$, acquired by measuring the ratio between the raw digitizer units and the voltage amplitude of the ≈ 15 MHz sine wave (≈ 10 mV) injected into receiver. Amplitudes determined from (fig. S1), and significant figures reflect variance of multiple measurements.

Spectral width (kHz)	Receiver Calibration ($\text{dg} / \mu\text{V}$)
3.9	476.4
40	727.8
200	583.0
1000	466.1
4000	117.7
10000	49.73
75000	6.0

Put a number on “multiple” above – also, why is the 75 MHz number lower precision than the others? Do you have it higher precision? If not, just leave it alone, but it seemed like you might.

there’s redundancy between the figure caption and the text

Test signal with a voltage amplitude of 15.21 mV and a frequency of 14.9 MHz was generated by injecting about $1 V_{amp}$ into 2 calibrated attenuator blocks through the receiver chain. The signal amplitude was verified first by acquiring on an oscilloscope. The test signal was acquired at the set spectral widths (in the case of fig. S1 - 200kHz) with four transients on the SpinCore transceiver

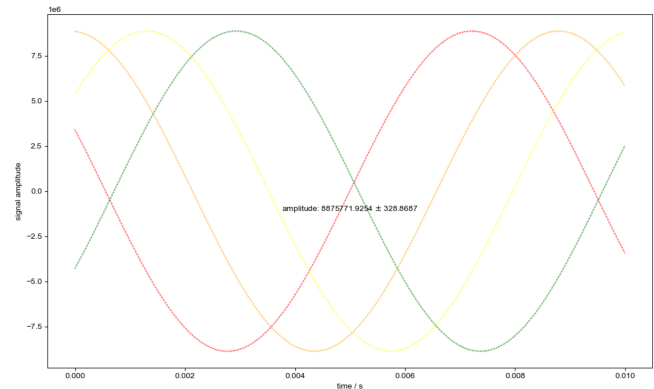


FIG. S1. Test signal with a voltage amplitude of 15.21 mV was injected to the SpinCore transceiver board and 4 transients were collected using a spectral width of 200 kHz and fit to a sinusoidal waveform to extract an amplitude of 8875771.9254 in arbitrary units assigned by the transceiver board

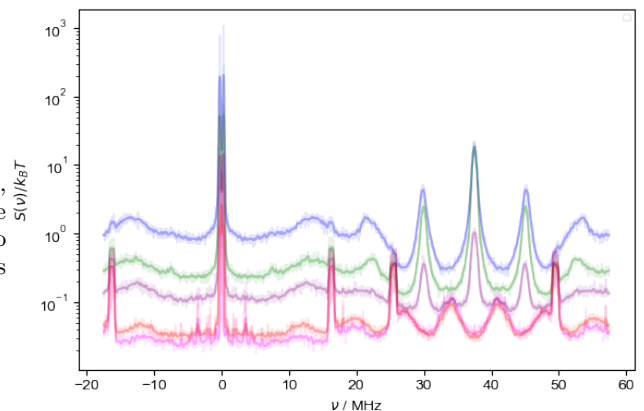


FIG. S2. A variable attenuator with 3 dB (blue), 10 dB (green), 13 dB (purple), and 23 dB (red) was placed between the output of the terminated receiver chain and the input of the SpinCore. The terminated SpinCore (magenta) is shown as a reference. Both the noise and high frequency harmonics scale with attenuation up to 13 dB. At 23 dB the oscillations shift frequency and resemble the terminated SpinCore PSD.

board and each fit to a sinusoidal wave. The final receiver calibration factor was determined by taking the ratio of the real voltage value of the injected test signal to the average amplitude of the four captured transients.

S2.2. High-frequency Noise of Transceiver

After observing the higher frequency oscillations in fig. ??, the PSD was further investigated by varying the attenuation between the output of the receiver chain and the input of the transceiver board.

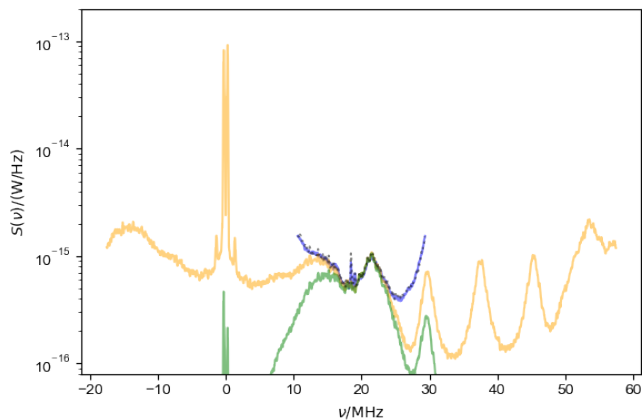


FIG. S3. The PSD acquired on the transceiver board with a spectral width of 75 MHz (gold) is multiplied by a sinc function appropriate for a dataset with a spectral width of 20 MHz to yield a filtered noise PSD (green). This product is then downsampled to produce the predicted noise PSD for a spectrum taken with a spectral width of 20 MHz (dashed black). The actual acquired spectra (blue) having a spectral width of 20 MHz shows the exact same aliasing and shape as the predicted model. At such a wide spectral width a large convolution filter width of 100 kHz is required to smooth out the noise peaks (not shown)

S2.3. Predicting wide spectral width PSD

In addition to smaller spectral widths, the broadest spectral widths (75 MHz and 20 MHz) were also acquired and compared to the predicted noise PSD based on the digital filter of the transceiver board. Even transitioning from the maximal digitizing rate to a 20 MHz spectral width is accurately predicted using the digital filter expected for a dataset with a spectral width of 20 MHz (fig. ??).

Using the spectral widths of 75 MHz and 20 MHz the spikes seen with higher resolution are not apparent as they are in fig. 13.

S2.4. Quantification of Gain

The gain of the receiver pathway was calculated by outputting a measured test signal over a range of rf frequencies into the receiver pathway and the amplified noise was collected on the oscilloscope (fig. S4).

The plot of measured test signal indicates a fairly consistent amplitude output of the AFG, while the output power of the spectrometer shows a clear rise in power at a frequency of 12.5 MHz. This trend in gain variation is most likely due to the analog components of the receiver chain (e.g., the included pi circuits and tuned limiter) acting as additional filters. This measurement is key to properly quantifying the signal and noise in later steps to calculate the signal directly at the output of the probe.

S2.5. Nutation Curve (Measurement of Λ)

To acquire the 90 time of the coil, a simple nutation experiment was run with a pulse times ranging from 0.5

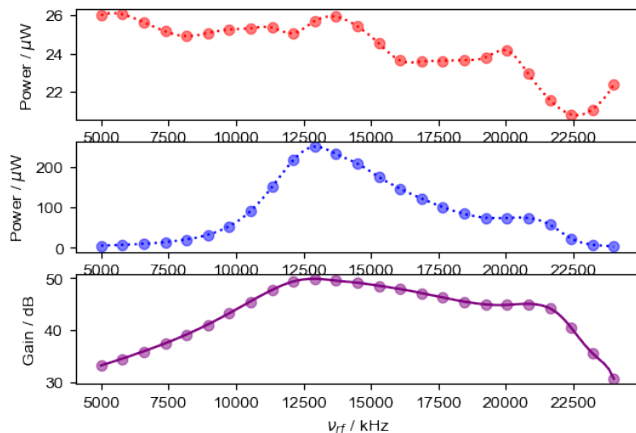
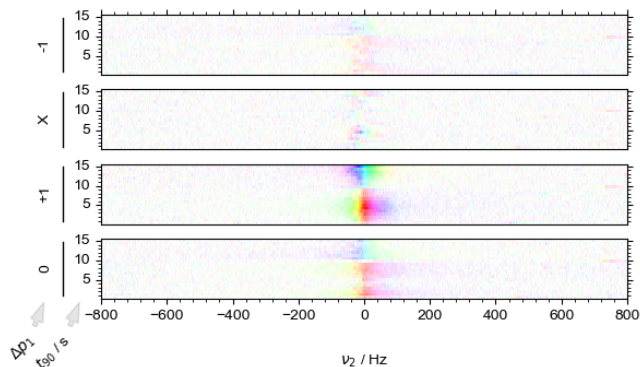


FIG. S4. A) Test signal output from the AFG and directly input to the oscilloscope and fit to a cubic spline. B) Output of the receiver chain when the test signal shown in A is injected into a 40.0210 dB attenuator attached to the input of the receiver chain, as measured by the oscilloscope. C) Gain in dB calculated with the attenuator taken into consideration, as a function of the input frequency.

to 15.5 μ s with a four step phase cycle on the ninety pulse. The integrated data was then fit to a sinusoidal wave that indicates a peak at 4.52 μ s. A domain colored coherence transfer pathway validates this ninety time by showing a clear inversion from red to blue in the same pulse time.

here, include the color wheel on top of the plot in inkscape



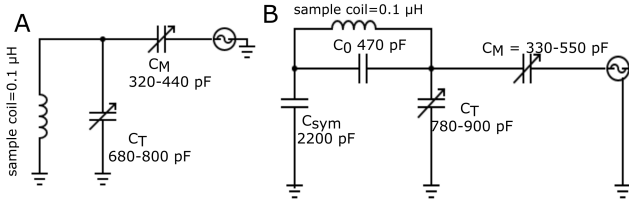
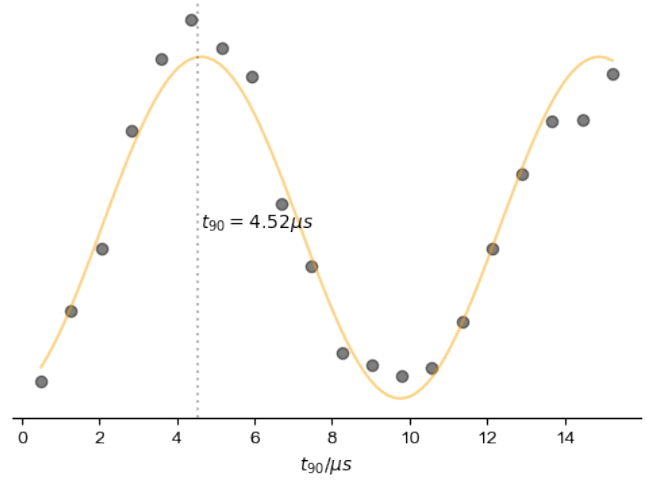
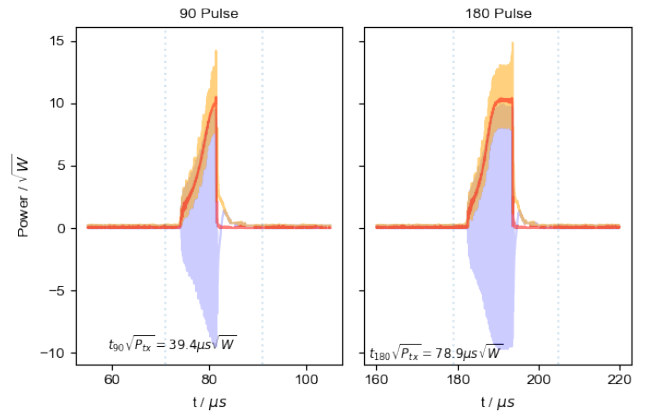


FIG. S5. Comparison of the two probe circuits. A) The “single sided” tank circuit consists of a tuning capacitance (C_T) and matching capacitance (C_M). Both include 120 pF variable capacitors in order to span the ranges specified in the figure. The double hairpin coil with a volume of $8.55 \mu\text{L}$ has an inductance of $\sim 0.1 \mu\text{H}$ measured with a miniVNA. B) The circuitry used for the balanced probe includes two additional capacitors. Both coils are double hairpins with a volume of $8.55 \mu\text{L}$ and an inductance around $\sim 0.1 \mu\text{H}$



Using the ninety pulse time of $4.52 \mu\text{s}$ a typical Hahn echo was captured via the oscilloscope. The acquired data was frequency filtered and converted to analytic signal and the integral of the absolute signal for the ninety pulse shows a. an imperfect rise time of the pulse and b. a total $t_{90}\sqrt{P_{tx}} = 39.4 \mu\text{s}\sqrt{W}$ (fig. ??).



S2.6. Probe Circuit Diagrams